

## Article

# Design and Characterization of Nanostructured Ag<sub>2</sub>O-Ag/Au Based on Al<sub>2</sub>O<sub>3</sub> Template Membrane for Photoelectrochemical Water Splitting and Hydrogen Generation

Huda Mostafa <sup>1,2</sup>, Ashour M. Ahmed <sup>2,3</sup>, Mohamed Shaban <sup>2,4</sup> , Ahmed A. Abdel-Khaliek <sup>1</sup>, Fuead Hasan <sup>5</sup> , Fatimah Mohammed Alzahrani <sup>6,\*</sup>  and Mohamed Rabia <sup>2,7,\*</sup> 

- <sup>1</sup> Physical Chemistry Laboratory, Chemistry Department, Faculty of Science, Beni-Suef University, Beni-Suef 62514, Egypt
  - <sup>2</sup> Nanophotonics and Applications Laboratory, Physics Department, Faculty of Science, Beni-Suef University, Beni-Suef 62514, Egypt
  - <sup>3</sup> Physics Department, College of Science, Imam Mohammad Ibn Saud Islamic University (IMSIU), Riyadh 11623, Saudi Arabia
  - <sup>4</sup> Department of Physics, Faculty of Science, Islamic University of Madinah, Madinah 42351, Saudi Arabia
  - <sup>5</sup> Nanoscale Science, University of North Carolina at Charlotte, Charlotte, NC 28223, USA
  - <sup>6</sup> Chemistry Department, College of Science, Princess Nourah Bint Abdulrahman University, Riyadh 11671, Saudi Arabia
  - <sup>7</sup> Nanomaterials Science Research Laboratory, Chemistry Department, Faculty of Science, Beni-Suef University, Beni-Suef 62514, Egypt
- \* Correspondence: fmalzahrani@pnu.edu.sa (F.M.A.); mohamedchem@science.bsu.edu.eg (M.R.)



**Citation:** Mostafa, H.; Ahmed, A.M.; Shaban, M.; Abdel-Khaliek, A.A.; Hasan, F.; Mohammed Alzahrani, F.; Rabia, M. Design and Characterization of Nanostructured Ag<sub>2</sub>O-Ag/Au Based on Al<sub>2</sub>O<sub>3</sub> Template Membrane for Photoelectrochemical Water Splitting and Hydrogen Generation. *Photonics* **2022**, *9*, 968. <https://doi.org/10.3390/photonics9120968>

Received: 24 October 2022

Accepted: 2 December 2022

Published: 11 December 2022

**Publisher's Note:** MDPI stays neutral with regard to jurisdictional claims in published maps and institutional affiliations.



**Copyright:** © 2022 by the authors. Licensee MDPI, Basel, Switzerland. This article is an open access article distributed under the terms and conditions of the Creative Commons Attribution (CC BY) license (<https://creativecommons.org/licenses/by/4.0/>).

**Abstract:** This study considers the progress of our previous study for hydrogen generation depends on the highly ordered metal oxide/plasmonic materials. This study reports the preparation of Ag<sub>2</sub>O-Ag/Au on the Al<sub>2</sub>O<sub>3</sub> template (Ag<sub>2</sub>O-Ag/Au/Al<sub>2</sub>O<sub>3</sub>) for photocatalytic sewage water splitting and H<sub>2</sub> gas production. Ni imprinting, followed by two-step anodization procedures, prepare the Al<sub>2</sub>O<sub>3</sub> template. Ag<sub>2</sub>O-Ag and Au materials are prepared inside the template using electrochemical deposition and sputter coating methods, respectively. The chemical structure is confirmed by X-ray diffraction (XRD) and X-ray photoelectron spectroscopy (XPS) analyses, in which all the peaks characterized by Ag<sub>2</sub>O, Ag, Au, and Al<sub>2</sub>O<sub>3</sub> are confirmed. The scanning electron microscope (SEM) images confirm the preparation of a highly ordered hexagonal Al<sub>2</sub>O<sub>3</sub> template with a pore wide of about 350 nm. Ag<sub>2</sub>O-Ag/Au accept the same morphology after the deposition process, in which the materials are deposited inside and on the Al<sub>2</sub>O<sub>3</sub> template, in which the hexagonal pores are still opened after the deposition process. These open pores increase the surface area and then enhance the optical and electrical properties. For the H<sub>2</sub> generated from sewage water, the produced Ag<sub>2</sub>O-Ag/Au on the Al<sub>2</sub>O<sub>3</sub> photoelectrode achieved an incident to photon conversion efficiency (IPCE) of 30%. Additionally, the impact of light wavelength and intensity on photoelectrode performance is evaluated. Under increasing the light total power from 25 to 75 mW.cm<sup>-2</sup>, the current density (J<sub>ph</sub>) value goes up from 8.9 to 9.5 mA.cm<sup>-2</sup>. The current study's findings show promising results for resolving the issue of energy in remote areas by turning wastewater into hydrogen fuel.

**Keywords:** aluminum template; nanoporous; photoelectrode; sewage water; hydrogen generation; water splitting

## 1. Introduction

Under the reduction in nonrenewable energy sources, scientists do their best for providing additional sources that are called renewable energy [1]. Through the development of these new sources, photocatalytic materials consider promising factors for the enchantment of these sources [1–4].

One of the cheapest and most applicable renewable energy sources is H<sub>2</sub> gas. Through the application of photocatalytic materials, researchers can produce this gas from different electrolytes such as acids and basics. This gas has different applications in our life, it can be used as a fuel for airplanes, aircraft, and cars. Moreover, many factories and companies use this gas as a fuel instead of fossil fuel. Through the reduction of using fossil fuels, emitting dangerous gases such as CO<sub>x</sub>, NO<sub>x</sub>, and SO<sub>x</sub> are decreased in our environment [5–7].

For the H<sub>2</sub> generation reaction, it is essential for photocatalysts to be semiconductor materials like metal oxides, nitrides, sulfides, or organic compounds [8,9]. Due to their stability, low cost, high efficiency, and simplicity of preparation, metal oxides are excellent photocatalytic materials for the generation of H<sub>2</sub> gas [10,11]. Increasing the surface area (through nanofibers, nanowires, and nanotubes) is one way to improve photocatalytic activity [12–14]. Materials that are plasmonic [15,16] or have a high thermal capacity are another option to increase the photocatalytic activity such as Ag or Au which is considered one of the top 10 thermally conductive materials with values of 429 and 315 W/m•K, respectively. These materials effectively capture light, allowing the spread of electron localization phenomena across composite semiconductor materials, that are then utilized by neighboring materials for the generation of H<sub>2</sub> [17]. Previous studies studied that to increase PCE from 14.8% to 17.5% and light harvesting efficiency, various Ag and Au forms were also added to TiO<sub>2</sub> [18]. Ag<sub>2</sub>O has a bandgap value in the range of 1.6 eV, making it a promising material for use in renewable energy [19]. These materials' low bandgap values make it possible for them to absorb the majority of solar light, which is preferred to big bandgap semiconductors, which can only absorb 10 to 20% of the light [20]. Additionally, Ag<sub>2</sub>O's decreased bandgap and excellent absorption efficiency support its use of renewable energy field. The preparation of materials in high order opens the fields of applications, in which these materials can be applied in optoelectronic devices, batteries, and electrodes for water-splitting reactions. Our team has studied the application of a template as a pH sensor for the detection of the H<sup>+</sup> ion concentration in solutions. The great pore order increases the sensitivity very much [21].

The previous studies carried out for water splitting still have some problems that are related to using small produced J<sub>ph</sub> values and then the IPCE. Moreover, all the previous studies used additional electrolytes for water-splitting reactions such as acids, bases, or salts.

This study considers the progress of our previous study for hydrogen generation depends on highly ordered metal oxide/plasmonic materials [22]. Ag<sub>2</sub>O-Ag/Au/Al<sub>2</sub>O<sub>3</sub> photoelectrode is prepared using different methods: electrochemical deposition, sputter coating, Ni imprinting, and two-step anodization methods. The optical properties, morphologies, and chemical structures of these materials are confirmed using different analytical tools: XRD, XPS, SEM, and UV-Vis devices. The electrochemical measurements are carried out by measuring the water-splitting reaction under dark/light, monochromatic light, and different light intensities.

## 2. Experimental Part

### 2.1. Aluminum Oxide Template Preparation

The Ni imprinting method was used to make a porous aluminum oxide template. The shallow arrays of the Ni mold exhibit a 400 nm-spaced hexagonal nanopillar structure. Al foil was polished using an electropolishing technique using a C<sub>2</sub>H<sub>5</sub>OH: HClO<sub>4</sub> (1v:1v) solution. By using an oil pressing machine for 3 min at 10 kN/cm<sup>2</sup>, 99.99% of the imprinted aluminum foil was produced. After that, a two-step anodization process using an electrolyte of ethylene glycol:H<sub>3</sub>PO<sub>4</sub>: H<sub>2</sub>O (100v:1v:200v) took conducted at 2 °C for 15 and 120 min, respectively. After the first anodization, the chemical etching process was carried out using a mixture of H<sub>3</sub>PO<sub>4</sub> (6 wt.%) and H<sub>2</sub>CrO<sub>4</sub> (1.5 wt.%) for 12 h at 60 °C. Lastly, to complete Al<sub>2</sub>O<sub>3</sub> synthesis, the pore siding is carried out using 6 wt.% H<sub>3</sub>PO<sub>4</sub> at 60 °C for 30 min.

## 2.2. Preparation of $\text{Ag}_2\text{O-Ag/Au/Al}_2\text{O}_3$

The electrodeposition technique is used to prepare of  $\text{Ag}_2\text{O-Ag}$  using the PowerStation (CHI660E) from solution 0.1M  $\text{AgNO}_3$  and 0.15 M boric acid ( $\text{H}_3\text{BO}_3$ ). First, 5 nm thin film Au nanoparticles are sputter inside the template using the sputter coater device. This step accepts the template and its conductivity. Then, the electrodeposition is carried out for 10 s, this led to the deposition of Ag inside the template. For the preparation of  $\text{Ag}_2\text{O}$ , the  $\text{Ag/Au/Al}_2\text{O}_3$  is combusted in the air at  $400^\circ\text{C}$  for 2 h. This process led to the preparation of  $\text{Ag}_2\text{O-Ag/Au/Al}_2\text{O}_3$ .

## 2.3. Characterization

Analyses of X-ray photoelectron spectroscopy and X-ray diffraction patterns (XRD) are used to verify the chemical structure. Utilizing Cu  $\text{K}\alpha$  radiation with a wavelength of 0.15418 nm on a Bruker D8 Advance diffractometer, XRD investigations were performed. The confirmation of chemical structure is carried out using XPS analysis, XPS, (K-ALPHA, USA). To evaluate the morphology, Hitachi's S-4800 (FE-SEM) was used. Using a double-beam spectrophotometer, the optical characteristics were investigated (Perkin Elmer Lambda 950, Waltham, MA, USA).

## 2.4. Electrochemical Measurements

Using a cell with three electrodes, the basic electrode ( $\text{Ag}_2\text{O-Ag/Au/Al}_2\text{O}_3$  nanomaterial) represents the working electrode, while a sheet of graphite (with the same size) and calomel represent the counter and reference electrodes, respectively. The  $\text{H}_2$  production reaction from sewage water solution was carried out. A Xenon lamp served as a solar simulator for all measurements, which were performed using a workstation (CHI660E, USA) with a potential range of  $-1$  to  $1$  V. Light wavelength (390 to 636 nm), light intensity ( $25$  to  $100\text{ mW}\cdot\text{cm}^{-2}$ ), and the performance of the electrode in dark and light conditions were some of the parameters that were examined (Figure 1).

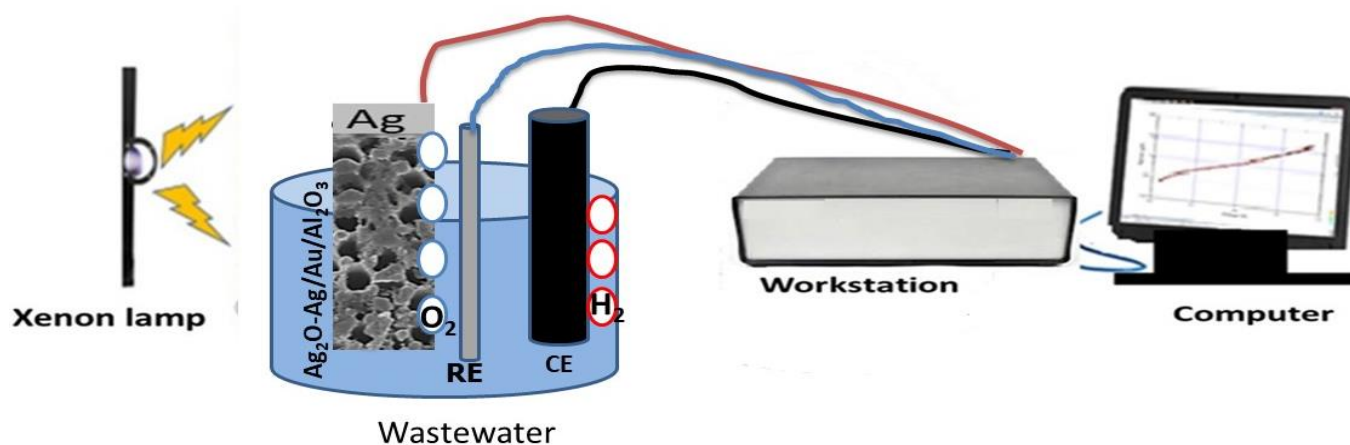


**Figure 1.** Diagram of the photoelectrochemical process for sewage water splitting reaction, in which  $\text{Ag}_2\text{O-Ag/Au/Al}_2\text{O}_3$  is the working electrode (WE), graphite is the counter electrode (CE), and calomel is the reference electrode (RE).

## 3. Results and Discussion

### 3.1. Characterization and Analyses

The X-ray diffraction pattern (XRD) of the  $\text{Al}_2\text{O}_3$  template and  $\text{Ag}_2\text{O-Ag/Au/Al}_2\text{O}_3$  nanomaterial is shown in Figure 2. This analysis clearly shows three peaks obtained for the  $\text{Al}_2\text{O}_3$  template at  $44.7^\circ$ ,  $64.9^\circ$ , and  $78.4^\circ$  which represent (113), (214), and (119), respectively (JCPDS card # 711123) [23]. These peaks confirm the polycrystalline structure of the  $\text{Al}_2\text{O}_3$  template. This appears well through the peaks at the growth direction (119) high intensity that indicates good crystallization in this orientation. Hence, the Ni-imprinting technique can easily fabricate the crystalline  $\text{Al}_2\text{O}_3$  template. The XRD of  $\text{Ag}_2\text{O-Ag/Au/Al}_2\text{O}_3$

shows six peaks, three of them at the same location and there are additional new peaks that appear after the electrodeposition and combustion processes. The XRD of the formed Ag nanoparticles is confirmed through several Bragg reflections of two peaks that were observed at  $2\theta$  values of  $38.0^\circ$ , and  $64.5^\circ$  which are indexed to (111), (220) planes of pure silver with the cubic-phase crystal system (JCPDS NO. 04-0783) [24,25]. Also, the Au has three peaks at  $44.7^\circ$ ,  $65^\circ$ , and  $78.1^\circ$  for the growth directions (111), (200), and (311) which matched with the previous literature [26,27].  $\text{Ag}_2\text{O}$  has one peak at  $38^\circ$  for the growth direction (200), this matched with (JCPDS 76-1393) [28].

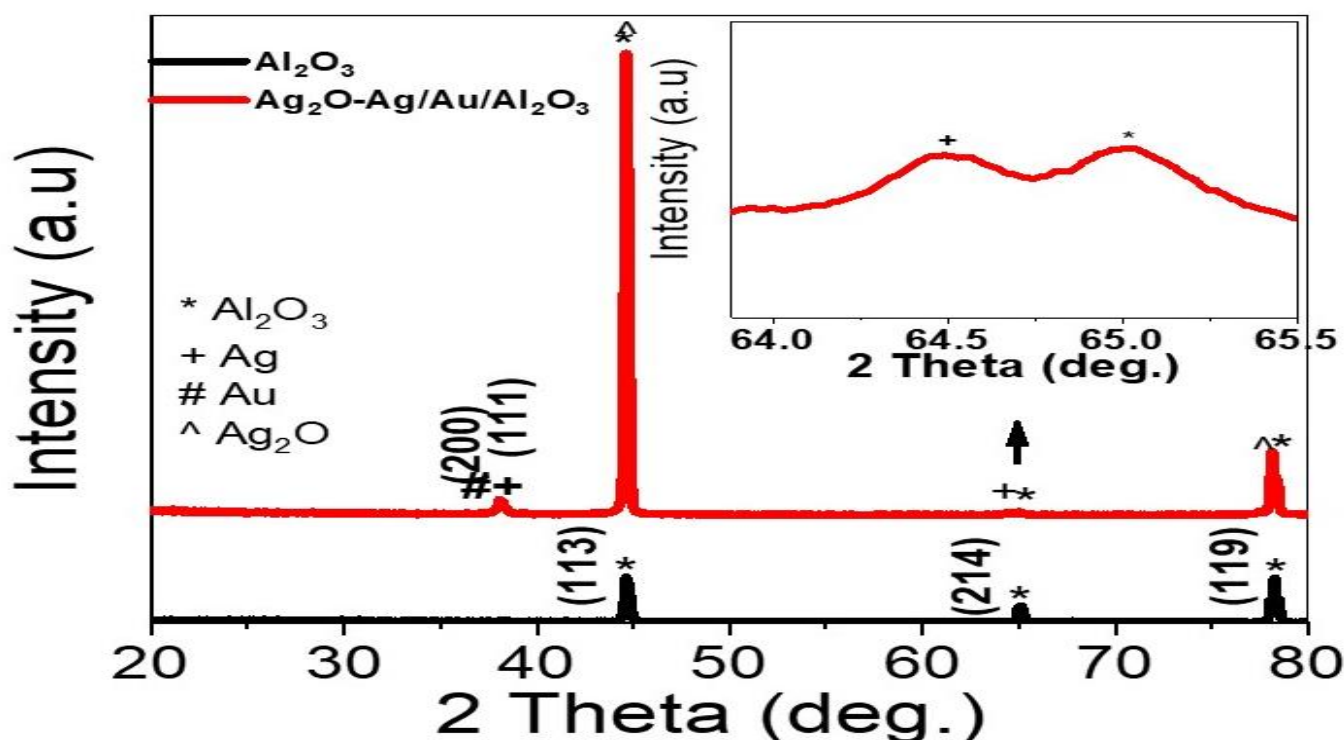


Figure 2. The XRD of  $\text{Al}_2\text{O}_3$  template and  $\text{Ag}_2\text{O-Ag/Au/Al}_2\text{O}_3$  nanomaterial.

To further support the prepared chemical's structure  $\text{Ag}_2\text{O-Ag/Au/Al}_2\text{O}_3$  nanomaterials, the sample is subjected to XPS analysis. The representation of the broad scanning profile for this sample when the binding is present between 850 and 50 eV in terms of energy is shown in Figure 3a. Strong highlighted signals were visible in the spectra of Ag 3d, O 1s, Au 4f, and Al 2p3. In more detail, the narrow scan is performed in better detail to fully explain each element's binding energy as well as the purification of the compounds (Figure 3b–e). Figure 3b shows that a dominating peak is seen at 532 eV, which is equivalent to the energy state of O 1s that relates to the lattice oxygen of  $\text{Ag}_2\text{O}$  and  $\text{Al}_2\text{O}_3$ . The Ag 3d spectrum peaks at 368 and 374 eV in the energy states of Ag 3d<sub>5/2</sub> and Ag 3d<sub>3/2</sub> for the Ag element, respectively [29,30], as shown in Figure 3c.

The spectra of Al 2p allow observing one broad peak (Figure 3d) at an electron binding energy of 75 eV, which is related to the alumina template. Finally, a detailed spectrum of the Au 4f core at the level depicted in Figure 3e can be described by two peaks Au 4f<sub>7/2</sub> and Au 4f<sub>5/2</sub> spin–orbit coupling peaks for Au, in which these peaks are located at 84 and 87.3 eV binding energy that confirm the plasmonic nature of Au [31].

Figure 4a,b illustrates the SEM of the  $\text{Al}_2\text{O}_3$  template before and after pore widening with  $\text{H}_3\text{PO}_4$  solution (6 wt.%  $\text{H}_3\text{PO}_4$  at  $60^\circ\text{C}$  for 30 min.). From these figures, the prepared template has very ordered pores that increase from 250 nm to 305 nm after the pore-widening process. At the same time, the interposes-distances decrease from 180 nm to 65 nm. The optimum  $\text{Al}_2\text{O}_3$  template (305 nm pore) is used as a template for the  $\text{Ag}_2\text{O-Ag/Au}$  nanomaterials as shown in Figure 4c,d under different magnifications. Moreover,

the optimum thickness for the template is 1.2  $\mu\text{m}$ . The  $\text{Ag}_2\text{O-Ag/Au}$  thin disordered layer is arrayed on a hexagonal arrangement as same for the  $\text{Al}_2\text{O}_3$  template. It clearly shows that  $\text{Ag}_2\text{O-Ag}$  covers the walls of the template very well, in which the pore diameter and interpore distance are about 240 and 140 nm, respectively. On the other hand, most of the pores are still open, this indicates the  $\text{Ag}_2\text{O-Ag}$  accepts tube shapes. These promising materials are expected to have great optical properties and then work as an excellent photoelectrode for additional water-splitting reactions.

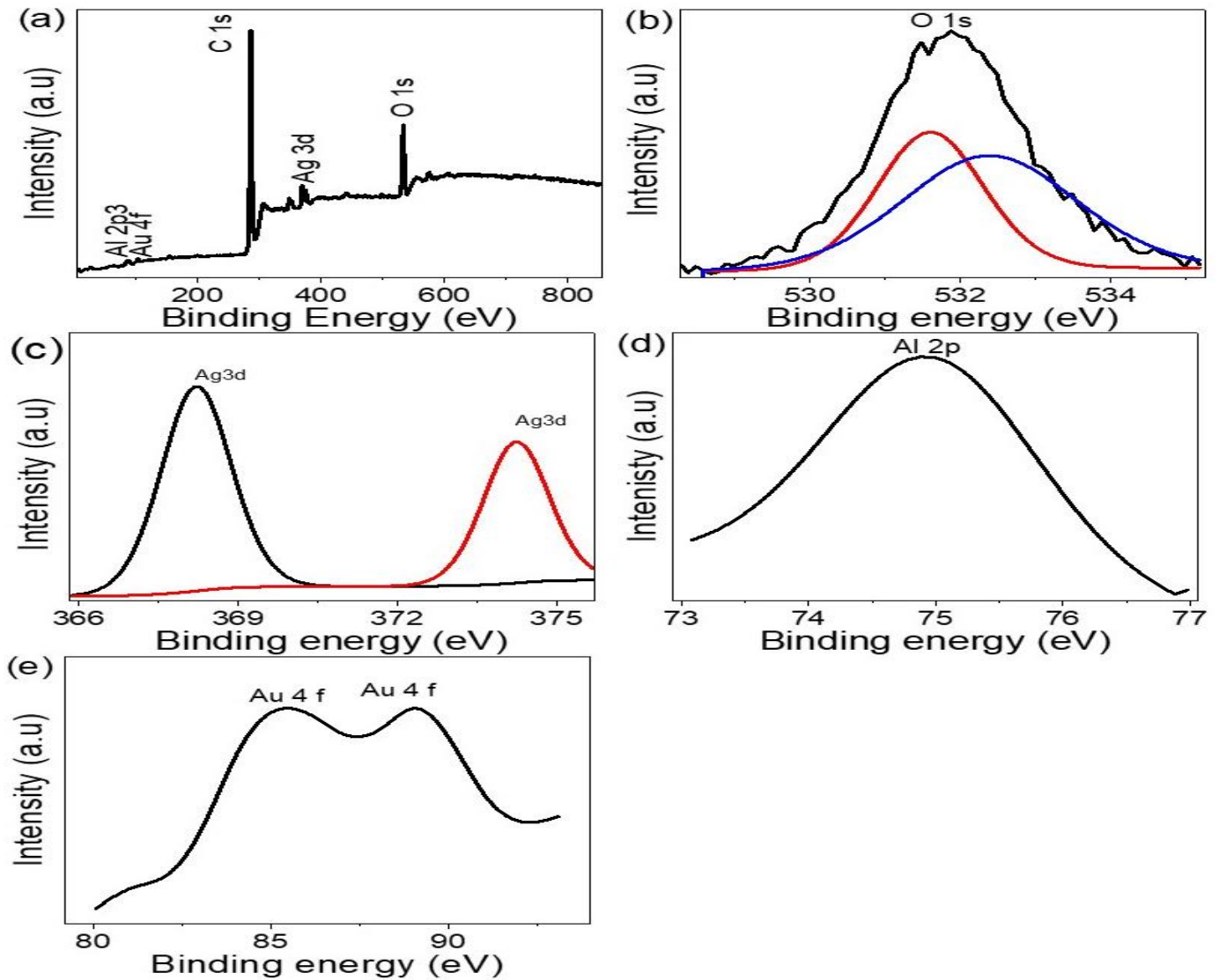


**Figure 3.** XPS analyses (a) survey, (b) O element, (c) Ag element, (d) Al element, and (e) Au element for the prepared  $\text{Ag}_2\text{O-Ag/Au/Al}_2\text{O}_3$  nanomaterials.

The UV–Vis spectrophotometer’s reflection plot as a response to the wavelength is displayed in Figure 5a. In the case of the  $\text{Al}_2\text{O}_3$  template, the optical reflectance value matches with the appearance of small interference fringes, this phenomenon is a result of the oscillation and interference of light after getting up from the pores [32]. After the deposition of  $\text{Ag}_2\text{O-Ag/Au}$  on and inside the template’s pores, there are enhancements in the optical behavior. The optical reflectance decreases as a result of increasing the absorbance behavior [31]. This appears from the decrease in the optical reflectance behavior. In these conditions, the interference fringes increase, this indicates the great interference of photons through the nanomaterials.

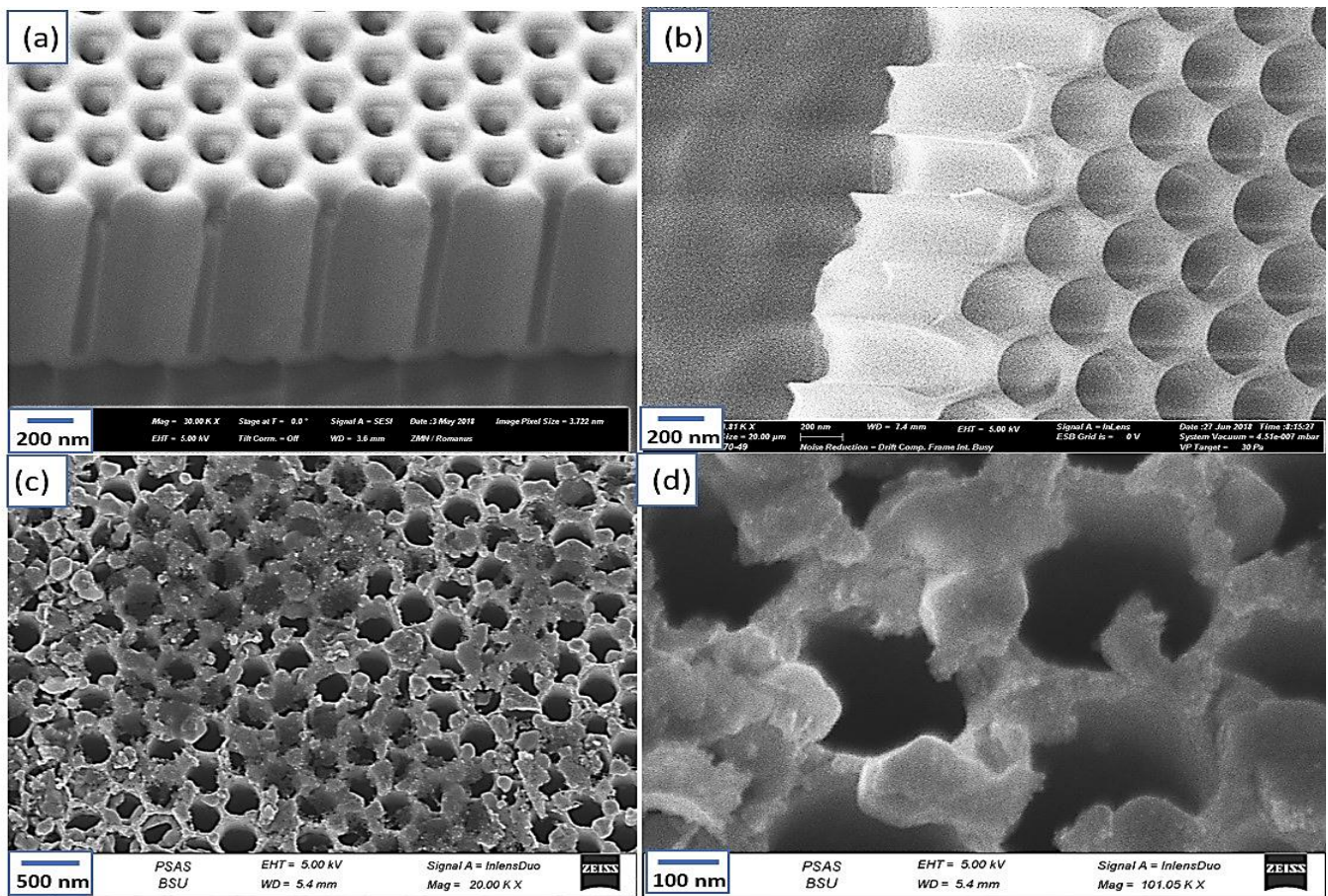


Figure 4. SEM of  $\text{Al}_2\text{O}_3$  template (a) before and (b) after pore widening. SEM of (c,d)  $\text{Ag}_2\text{O-Ag/Au}$  on the  $\text{Al}_2\text{O}_3$  template under different magnifications.

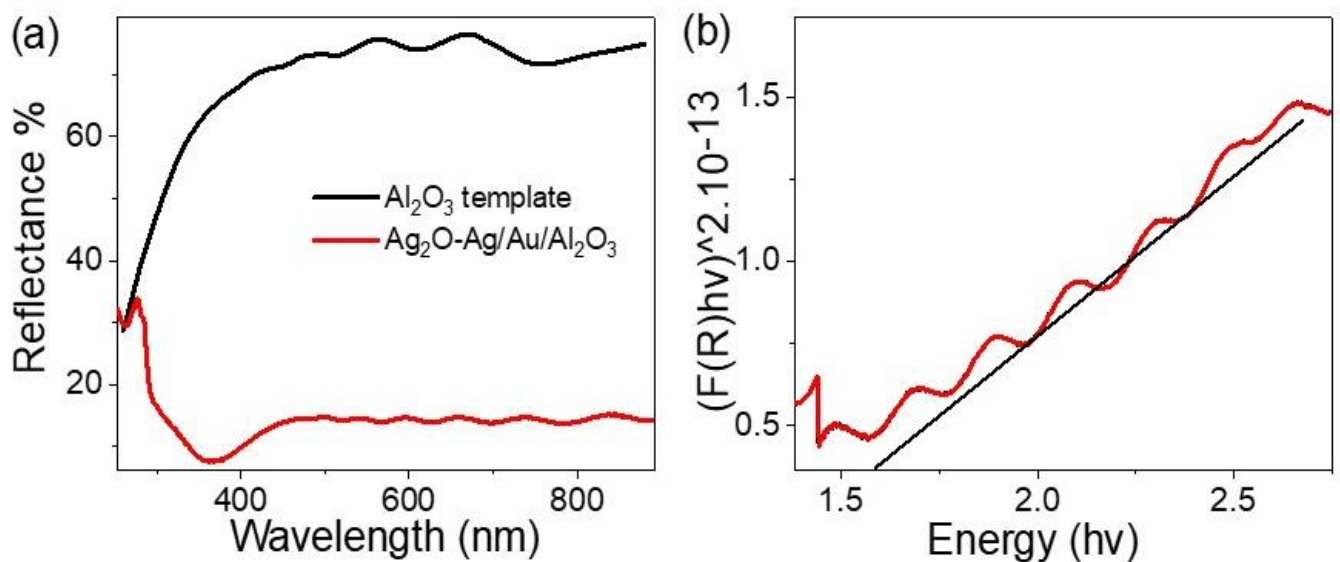


Figure 5. (a) Optical reflectance spectra of  $\text{Al}_2\text{O}_3$  and  $\text{Ag}_2\text{O-Ag/Au/Al}_2\text{O}_3$  and (b) band gap value of  $\text{Ag}_2\text{O-Ag/Au/Al}_2\text{O}_3$  nanomaterials.

The bandgap of the  $\text{Ag}_2\text{O-Ag/Au/Al}_2\text{O}_3$  nanomaterials is determined through the Kubelka–Munk equation (Equations (1)–(3)) [33]. This equation depends on  $K$ ,  $S$ , and  $R$ , which are the molar absorption coefficient, scattering factor, and the fraction of light

reflected from the nanomaterials, respectively. From this equation and Figure 5b, the bandgap of  $\text{Ag}_2\text{O-Ag/Au/Al}_2\text{O}_3$  nanomaterial is 1.56 eV.

It is evident that the prepared  $\text{Ag}_2\text{O-Ag/Au/Al}_2\text{O}_3$  nanomaterials have a high light absorption behavior in a wide optical range (Vis and near IR). This is related to the low reflectance behavior of  $\text{Ag}_2\text{O-Ag/Au/Al}_2\text{O}_3$  nanomaterials in these regions.

$$K = (1 - R)^2 \tag{1}$$

$$S = 2R \tag{2}$$

$$F(R) = K/S = \frac{(1 - R)^2}{2R} \tag{3}$$

### 3.2. The Electrochemical Measurements

The response of the  $\text{Ag}_2\text{O-Ag/Au/Al}_2\text{O}_3$  photoelectrode to the light intensity from 25 to  $75 \text{ mW.cm}^{-2}$  is shown in Figure 6. From this figure, the produced current per unit area represents the current density ( $J_{ph}$ ), this current is measured according to the calomel electrode as a reference electrode, then the current is drawn as a function of the reference hydrogen electrode (RHE).

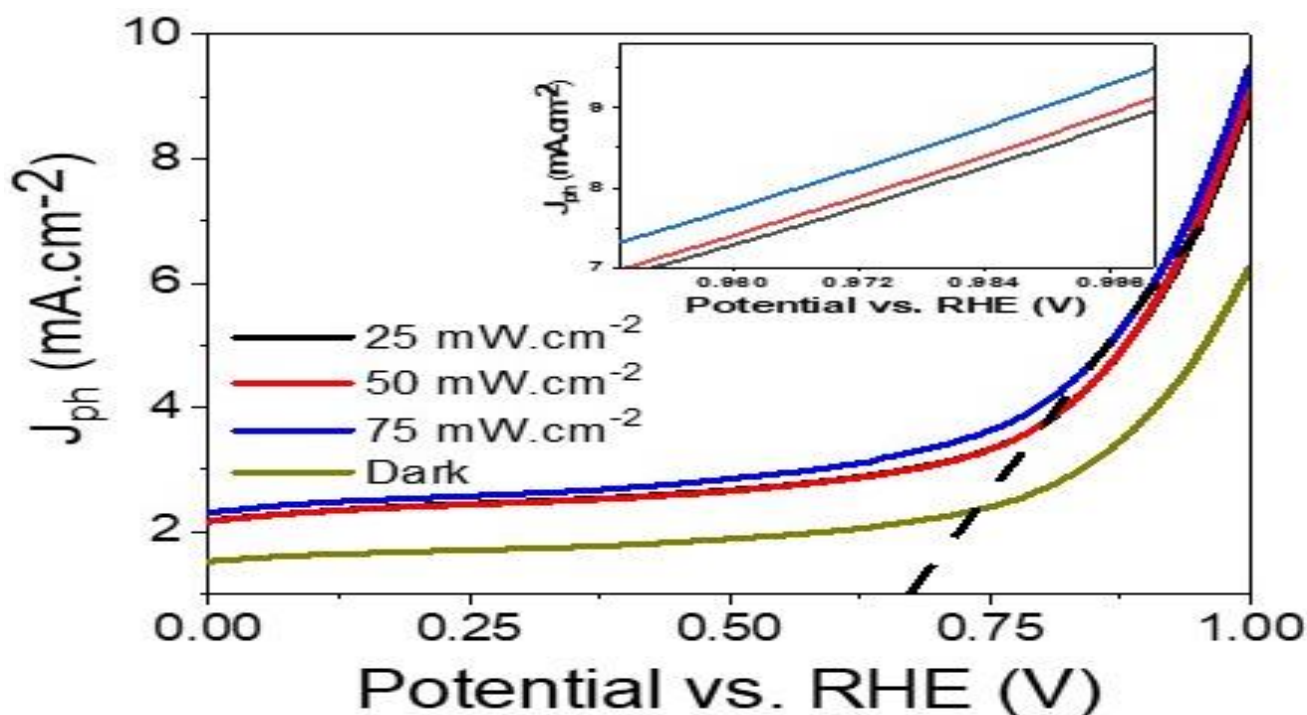


**Figure 6.** The relation between the potential and the current density (insert figure represents the magnification of the current density at 0.94 to 1.0 V) for the  $\text{Ag}_2\text{O-Ag/Au/Al}_2\text{O}_3$  photoelectrode.

From this figure, there is an increase in the  $J_{ph}$  values from 8.9 to 9.5 with an increase in the light intensity from 25 to  $75 \text{ mW.cm}^{-2}$ . The response of the photoelectrode to different light intensities shows the highly sensitive nature of the prepared photoelectrode to light intensity, in which the number of incident photons causes a motivation of a different number of electrons that collects and cause the generation of different  $J_{ph}$  values [34]. These electron–hole pairs are the main factors for the work of photocatalytic materials. From this process, the generated electrons are collected on the active sites of the photoactive materials [29,30].

The collected electrons appear as  $J_{ph}$  values that represent the water splitting rate and then the hydrogen generation percent [35,36]. In general, the light intensity (photons intensity) that are directly proportional to the photon’s numbers, as mentioned in

Equation (4) [33]. In which  $N$  is the number of photons,  $P$  is the light intensity,  $h$  is the Planck constant, and  $c$  is the light velocity. The  $N$  photons are changed from  $2 \times 10^{21}$  to  $6 \times 10^{21}$  photon/s with the light intensity from 25 to 75,  $\text{mW.cm}^{-2}$ , respectively.

$$N = \lambda P/hc \tag{4}$$

The response of the prepared  $\text{Ag}_2\text{O-Ag/Au/Al}_2\text{O}_3$  photoelectrode to the monochromatic light wavelength (390 to 636 nm) is shown in Figure 7a. Under the variation of the wavelength, the produced  $J_{\text{ph}}$  values change from 9.57 to 7.41  $\text{mA.cm}^{-2}$ , respectively. The relationship among wavelength values and the generated  $J_{\text{ph}}$  values at 1.0 V is shown in the insert figure which shows the decrease in  $J_{\text{ph}}$  values clearly.

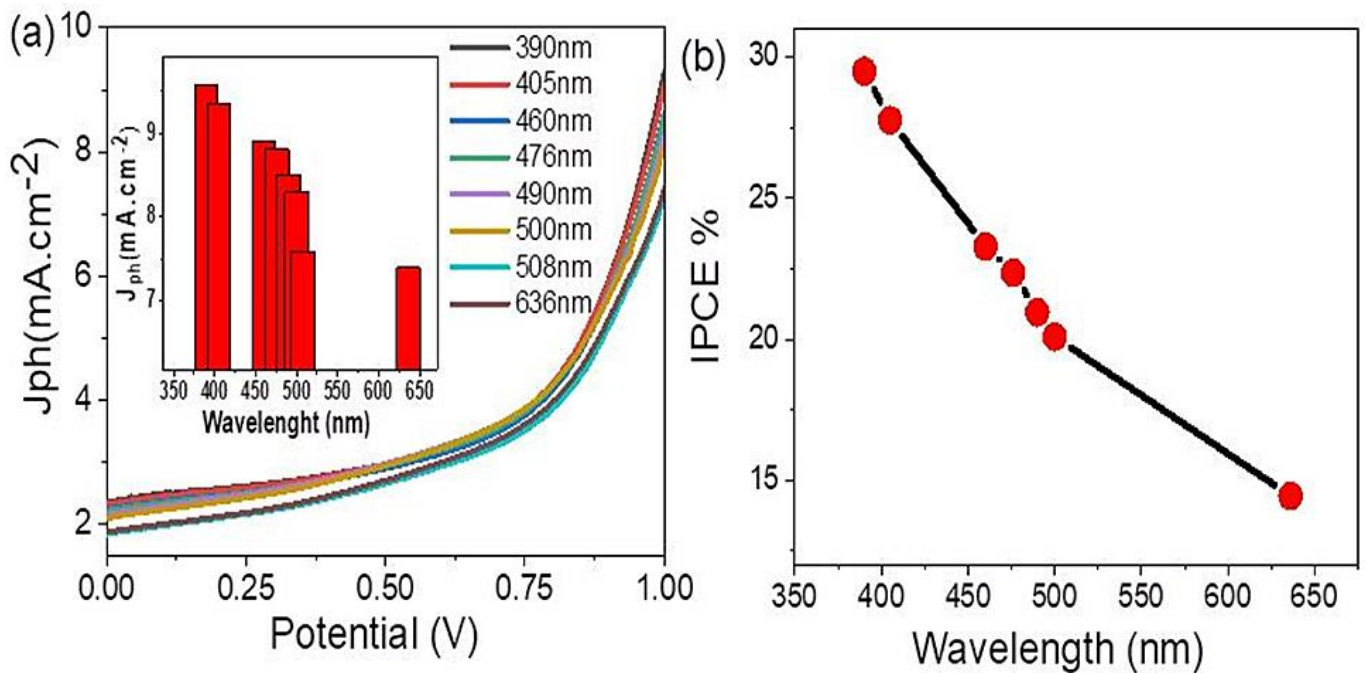


**Figure 7.** (a) The relation between the applied potential and the produced current density (the insert figure represents the relation between the applied wavelength and the produced current density at 1.0 V) and (b) the IPCE for the prepared  $\text{Ag}_2\text{O-Ag/Au/Al}_2\text{O}_3$  photoelectrode.

The efficiency of the hydrogen generation is shown in Figure 7b, this efficiency represents the incident photon to current conversion efficiency (IPCE), in which IPCE is calculated from Equation (5). And it depends on the parameters; wavelengths ( $\lambda$ ), current density, and light intensity ( $P$ ).

$$\text{IPCE} = \frac{J_{\text{ph}}(\text{mA.cm}^{-2}) \cdot 1240 (\text{V.nm})}{P(\text{mW.cm}^{-2}) \cdot \lambda(\text{nm})} \tag{5}$$

The IPCE values are 29.6 and 14.4 % at 390 and 636 nm, respectively. This indicates the water splitting and hydrogen generation reaction has the optimum values at the beginning of the visible region and then decreases till it reaches near IR.

The mechanism of the  $\text{Ag}_2\text{O-Ag/Au/Al}_2\text{O}_3$  photoelectrode for sewage water splitting reaction is produced under the effect of incidence photons and the response of the photoelectrode to these photons. The photoelectrode consists of semiconductor  $\text{Ag}_2\text{O}$  and plasmonic materials Ag and Au. So, the electron motion is carried out in steps, first, the light is captured through  $\text{Ag}_2\text{O}$ , Ag, and Au, in which the  $\text{Ag}_2\text{O}$  electrons transfer from the valency band to the conducting band. The second step is the localized surface plasmonic resonance (LSPR), the captured electrons through Ag and Au cause electron resonance through these plasmonic materials and then transfer to the neighbor  $\text{Ag}_2\text{O}$  semiconduc-

tor material. As a result of this process, the Ag<sub>2</sub>O material accumulates electrons. Then these electrons move to the electrolyte (sewage water) for the addition reaction of water splitting, in which both O<sub>2</sub> and H<sub>2</sub> gas are evolved on the anode and cathode surface, respectively. As a result of this reaction, J<sub>ph</sub> values are produced that represent the rate of the reaction [37,38]. Moreover, Table 1 confirms the improved behavior of the present study in comparison with previous literature.

**Table 1.** Comparison of the present study with previous literature through the used electrolyte, current density, and IPCE.

Photoelectrode	Electrolyte	J <sub>ph</sub> (mA/cm <sup>2</sup> )	IPCE % (390 nm)
g-C <sub>3</sub> N <sub>4</sub> -CuO [39]	NaOH	0.01	-
CuO thin films [40]	Na <sub>2</sub> SO <sub>4</sub>	0.96	3.1
CuO-C/TiO <sub>2</sub> [41]	glycerol	0.012	
CuO nanowire [42]	Na <sub>2</sub> SO <sub>4</sub>	1.5	-
TiO <sub>2</sub> /CdS/PbS [43]	Na <sub>2</sub> S/Na <sub>2</sub> S <sub>2</sub> O <sub>3</sub>	2	4
CuO nanostructure [44]	KOH	1	-
GaN [45]	HBr	0.6	8
SnO <sub>2</sub> /TiO <sub>2</sub> [46]	Na <sub>2</sub> S <sub>2</sub> O <sub>3</sub>	0.4	-
CuO nanocrystals [47]	Na <sub>2</sub> SO <sub>4</sub>	1.1	8.7
BiFeO <sub>3</sub> [48]	NaOH	0.1	0.21
ZnO/TiO <sub>2</sub> /FeOOH [49]	Na <sub>2</sub> S <sub>2</sub> O <sub>3</sub>	1.59	-
TiN-TiO <sub>2</sub> [50]	NaOH	3.0 × 10 <sup>-4</sup>	0.03
Au/PbS/Ro-GO/PANI [10]	Na <sub>2</sub> S <sub>2</sub> O <sub>3</sub>	1.1	10
Au/Pb(Zr, Ti)O <sub>3</sub> [51]	NaOH	0.06	0.2
PrFeO [52]	Na <sub>2</sub> SO <sub>4</sub>	0.130	-
Poly(3-aminobenzoic acid) frame [53]	H <sub>2</sub> SO <sub>4</sub>	0.08	-
PANI/Ag <sub>2</sub> O/Ag Nanocomposite [53]	Sewage water	0.012	-
Present work (Ag <sub>2</sub> O-Ag/Au/Al <sub>2</sub> O <sub>3</sub> )	Sewage water	9.5	29.6

#### 4. Conclusions

The use of an Ag<sub>2</sub>O-Ag/Au/Al<sub>2</sub>O<sub>3</sub> photoelectrode for the sewage water splitting reaction for O<sub>2</sub> and H<sub>2</sub> gas production shows promising results. All analyses are carried out to verify the Ag<sub>2</sub>O-Ag/Au/Al<sub>2</sub>O<sub>3</sub> photoelectrode's chemical composition, morphology, and optical characteristics. According to the SEM images, the produced materials contain nanoporous characteristics with hexagonal shapes of 305 nm diameter for the Al<sub>2</sub>O<sub>3</sub> template. This pore diameter decreases to 240 nm after Ag<sub>2</sub>O-Ag deposition. For Ag<sub>2</sub>O-Ag/Au/Al<sub>2</sub>O<sub>3</sub>, the bandgap is 1.56 eV which gives a promising feature for the light absorbance and photoelectrode water splitting reaction. Under increasing the light power density from 25 to 75 mW.cm<sup>-2</sup>, the J<sub>ph</sub> value changed from 8.9 to 9.5 mA.cm<sup>-2</sup>, respectively. The IPCE was altered by the influence of monochromatic light, in which, the IPCE values change from 29.6 and 14.4% at 390 and 636 nm, respectively. As the prepared photoelectrode has a great IPCE for the sewage water splitting reaction, our team will soon be working on a prototype for the fabrication of an electrochemical cell for water splitting and H<sub>2</sub> gas production.

**Author Contributions:** Conceptualization, H.M., A.M.A., M.S., A.A.A.-K. and M.R.; methodology, H.M., A.M.A., M.S., A.A.A.-K. and M.R.; software, H.M.; validation, F.M.A. and M.R.; formal analysis, M.R.; investigation, H.M., A.M.A., F.H., F.M.A. and M.R.; resources, H.M., A.M.A., M.S., A.A.A.-K., F.H., F.M.A. and M.R.; data curation, H.M., A.M.A., M.S., A.A.A.-K., F.H. and F.M.A., M.R.; writing—original draft preparation, H.M., A.M.A., M.S., A.A.A.-K., F.H., F.M.A. and M.R.; writing—review and editing, H.M., A.M.A., M.S., A.A.A.-K., F.H., F.M.A. and M.R.; visualization, H.M., A.M.A., M.S., A.A.A.-K., F.H., F.M.A. and M.R.; supervision, A.M.A., M.S., A.A.A.-K., F.M.A. and M.R.; project administration, H.M., F.M.A. and M.R.; funding acquisition, F.M.A. All authors have read and agreed to the published version of the manuscript.

**Funding:** The authors extend their appreciation to the Deanship of Scientific Research at Princess Nourah bint Abdulrahman University for funding this work through Princess Nourah bint Abdulrahman University Researchers Supporting Project number (PNURSP2022R42), Princess Nourah bint Abdulrahman University, Riyadh, Saudi Arabia.

**Institutional Review Board Statement:** Not applicable.

**Informed Consent Statement:** Not applicable.

**Conflicts of Interest:** The authors declare no conflict of interest.

## References

- Nishiyama, H.; Yamada, T.; Nakabayashi, M.; Maehara, Y.; Yamaguchi, M.; Kuromiya, Y.; Nagatsuma, Y.; Tokudome, H.; Akiyama, S.; Watanabe, T.; et al. Photocatalytic Solar Hydrogen Production from Water on a 100-M<sup>2</sup> Scale. *Nature* **2021**, *598*, 304–307. [[CrossRef](#)] [[PubMed](#)]
- Hisatomi, T.; Domen, K. Reaction Systems for Solar Hydrogen Production via Water Splitting with Particulate Semiconductor Photocatalysts. *Nat. Catal.* **2019**, *2*, 387–399. [[CrossRef](#)]
- Pagliaro, M. Preparing for the Future: Solar Energy and Bioeconomy in the United Arab Emirates. *Energy Sci. Eng.* **2019**, *7*, 1451–1457. [[CrossRef](#)]
- Takata, T.; Jiang, J.; Sakata, Y.; Nakabayashi, M.; Shibata, N.; Nandal, V.; Seki, K.; Hisatomi, T.; Domen, K. Photocatalytic Water Splitting with a Quantum Efficiency of Almost Unity. *Nature* **2020**, *581*, 411–414. [[CrossRef](#)] [[PubMed](#)]
- Mohamed, F.; Rabia, M.; Shaban, M. Synthesis and Characterization of Biogenic Iron Oxides of Different Nanomorphologies from Pomegranate Peels for Efficient Solar Hydrogen Production. *J. Mater. Res. Technol.* **2020**, *9*, 4255–4271. [[CrossRef](#)]
- Shaban, M.; Ali, S.; Rabia, M. Design and Application of Nanoporous Graphene Oxide Film for CO<sub>2</sub>, H<sub>2</sub> and C<sub>2</sub> H<sub>2</sub> Gases Sensing. *J. Mater. Res. Technol.* **2019**, *8*, 4510–4520. [[CrossRef](#)]
- Elsayed, A.M.; Rabia, M.; Shaban, M.; Aly, A.H.; Ahmed, A.M. Preparation of Hexagonal Nanoporous Al<sub>2</sub>O<sub>3</sub>/TiO<sub>2</sub>/TiN as a Novel Photodetector with High Efficiency. *Sci. Rep.* **2021**, *11*, 17572. [[CrossRef](#)]
- Kang, Z.; Cheng, Y.; Zheng, Z.; Cheng, F.; Chen, Z.; Li, L.; Tan, X.; Xiong, L.; Zhai, T.; Gao, Y. MoS<sub>2</sub>-Based Photodetectors Powered by Asymmetric Contact Structure with Large Work Function Difference. *Nano-Micro Lett.* **2019**, *11*, 34. [[CrossRef](#)]
- Lee, J.H.; Lee, W.W.; Yang, D.W.; Chang, W.J.; Kwon, S.S.; Park, W. II Anomalous Photovoltaic Response of Graphene-on-GaN Schottky Photodiodes. *ACS Appl. Mater. Interfaces* **2018**, *10*, 14170–14174. [[CrossRef](#)]
- Shaban, M.; Rabia, M.; El-Sayed, A.M.A.; Ahmed, A.; Sayed, S. Photocatalytic Properties of PbS/Graphene Oxide/Polyaniline Electrode for Hydrogen Generation. *Sci. Rep.* **2017**, *7*, 14100. [[CrossRef](#)]
- Rabia, M.; Mohamed, H.S.H.; Shaban, M.; Taha, S. Preparation of Polyaniline/PbS Core-Shell Nano/Microcomposite and Its Application for Photocatalytic H<sub>2</sub> Electrogeneration from H<sub>2</sub>O. *Sci. Rep.* **2018**, *8*, 1107. [[CrossRef](#)] [[PubMed](#)]
- Mohamed, H.S.H.; Rabia, M.; Zhou, X.G.; Qin, X.S.; Khabiri, G.; Shaban, M.; Younus, H.A.; Taha, S.; Hu, Z.Y.; Liu, J.; et al. Phase-Junction Ag/TiO<sub>2</sub> Nanocomposite as Photocathode for H<sub>2</sub> Generation. *J. Mater. Sci. Technol.* **2021**, *83*, 179–187. [[CrossRef](#)]
- Rabia, M.; Shaban, M.; Jibali, B.M.; Abdelkhaliek, A.A. Effect of Annealing Temperature on the Photoactivity of ITO/VO<sub>2</sub> (M)/Au Film Electrodes for Water Splitting. *J. Nanosci. Nanotechnol.* **2020**, *20*, 4120–4130. [[CrossRef](#)] [[PubMed](#)]
- Rabia, M.; Mohamed, S.H.; Zhao, H.; Shaban, M.; Lei, Y.; Ahmed, A.M. TiO<sub>2</sub>/TiOxNY Hollow Mushrooms-like Nanocomposite Photoanode for Hydrogen Electrogeneration. *J. Porous Mater.* **2019**, *27*, 133–139. [[CrossRef](#)]
- Zhang, X.; Li, J.; Yang, W.; Leng, B.; Niu, P.; Jiang, X.; Liu, B. High-Performance Flexible Ultraviolet Photodetectors Based on AZO/ZnO/PVK/PEDOT:PSS Heterostructures Integrated on Human Hair. *ACS Appl. Mater. Interfaces* **2019**, *11*, 24459–24467. [[CrossRef](#)] [[PubMed](#)]
- Kim, J.; Lee, H.C.; Kim, K.H.; Hwang, M.S.; Park, J.S.; Lee, J.M.; So, J.P.; Choi, J.H.; Kwon, S.H.; Barrelet, C.J.; et al. Photon-Triggered Nanowire Transistors. *Nat. Nanotechnol.* **2017**, *12*, 963–968. [[CrossRef](#)]
- Zhang, X.; Liu, Q.; Liu, B.; Yang, W.; Li, J.; Niu, P.; Jiang, X. Giant UV Photoresponse of a GaN Nanowire Photodetector through Effective Pt Nanoparticle Coupling. *J. Mater. Chem. C* **2017**, *5*, 4319–4326. [[CrossRef](#)]
- Cheng, Y.; Chen, C.; Chen, X.; Jin, J.; Li, H.; Song, H.; Dai, Q. Considerably Enhanced Perovskite Solar Cells via the Introduction of Metallic Nanostructures. *J. Mater. Chem. A* **2017**, *5*, 6515–6521. [[CrossRef](#)]

19. Samson, O.; Adeeko, T.O.; Makama, E.K. Synthesis and Optical Characterization of Silver Nanoparticles (Ag-NPs) Thin Films (TFs) Prepared by Silar Technique. *Int. J. Curr. Res. Acad. Rev.* **2017**, *5*, 15–24. [[CrossRef](#)]
20. Chiang, C.Y.; Shin, Y.; Aroh, K.; Ehrman, S. Copper Oxide Photocathodes Prepared by a Solution Based Process. *Int. J. Hydrogen Energy* **2012**, *37*, 8232–8239. [[CrossRef](#)]
21. Altowyan, A.S.; Shaban, M.; Gamel, A.; Gamal, A.; Ali, M.; Rabia, M. High-Performance PH Sensor Electrodes Based on a Hexagonal Pt Nanoparticle Array-Coated Nanoporous Alumina Membrane. *Materials* **2022**, *15*, 6515. [[CrossRef](#)] [[PubMed](#)]
22. Almohammed, A.; Shaban, M.; Mostafa, H.; Rabia, M. Nanoporous TiN/TiO<sub>2</sub>/Alumina Membrane for Photoelectrochemical Hydrogen Production from Sewage Water. *Nanomaterials* **2021**, *11*, 2617. [[CrossRef](#)] [[PubMed](#)]
23. Kumar, S.; Prakash, R.; Kumar, V. A Novel Yellowish White Dy<sup>3+</sup> Activated  $\alpha$ -Al<sub>2</sub>O<sub>3</sub> Phosphor: Photoluminescence and Optical Studies. *Funct. Mater. Lett.* **2015**, *8*, 1550061. [[CrossRef](#)]
24. Priyadharshini, R.I.; Prasannaraj, G.; Geetha, N.; Venkatachalam, P. Microwave-Mediated Extracellular Synthesis of Metallic Silver and Zinc Oxide Nanoparticles Using Macro-Algae (*Gracilaria Edulis*) Extracts and Its Anticancer Activity against Human PC3 Cell Lines. *Appl. Biochem. Biotechnol.* **2014**, *174*, 2777–2790. [[CrossRef](#)]
25. Meng, Y. A Sustainable Approach to Fabricating Ag Nanoparticles/PVA Hybrid Nanofiber and Its Catalytic Activity. *Nanomaterials* **2015**, *5*, 1124–1135. [[CrossRef](#)]
26. Krishnamurthy, S.; Esterle, A.; Sharma, N.C.; Sahi, S.V. Yucca-Derived Synthesis of Gold Nanomaterial and Their Catalytic Potential. *Nanoscale Res. Lett.* **2014**, *9*, 627. [[CrossRef](#)]
27. Sneha, K.; Sathishkumar, M.; Kim, S.; Yun, Y.S. Counter Ions and Temperature Incorporated Tailoring of Biogenic Gold Nanoparticles. *Process Biochem.* **2010**, *45*, 1450–1458. [[CrossRef](#)]
28. Ananth, A.; Mok, Y.S. Dielectric Barrier Discharge (DBD) Plasma Assisted Synthesis of Ag<sub>2</sub>O Nanomaterials and Ag<sub>2</sub>O/RuO<sub>2</sub> Nanocomposites. *Nanomaterials* **2016**, *6*, 42. [[CrossRef](#)]
29. Liu, L.; Sun, W.; Yang, W.; Li, Q.; Shang, J.K. Post-Illumination Activity of SnO<sub>2</sub> Nanoparticle-Decorated Cu<sub>2</sub>O Nanocubes by H<sub>2</sub>O<sub>2</sub> Production in Dark from Photocatalytic “Memory”. *Sci. Rep.* **2016**, *6*, 20878. [[CrossRef](#)]
30. Kim, Y.; Smith, J.G.; Jain, P.K. Harvesting Multiple Electron–Hole Pairs Generated through Plasmonic Excitation of Au Nanoparticles. *Nat. Chem.* **2018**, *10*, 763–769. [[CrossRef](#)]
31. Elsayed, A.M.; Shaban, M.; Aly, A.H.; Ahmed, A.M.; Rabia, M. Preparation and Characterization of a High-Efficiency Photoelectric Detector Composed of Hexagonal Al<sub>2</sub>O<sub>3</sub>/TiO<sub>2</sub>/TiN/Au Nanoporous Array. *Materials Science in Semiconductor Processing* **2022**, *139*, 106348. [[CrossRef](#)]
32. Ahmed, A.M.; Shaban, M. Nanoporous Chromium Thin Film for Active Detection of Toxic Heavy Metals Traces Using Surface-Enhanced Raman Spectroscopy. *Mater. Res. Express* **2020**, *7*, 015084. [[CrossRef](#)]
33. Hadia, N.M.A.; Abdelazeez, A.A.A.; Alzaid, M.; Shaban, M.; Mohamed, S.H.; Hoex, B.; Hajjiah, A.; Rabia, M. Converting Sewage Water into H<sub>2</sub> Fuel Gas Using Cu/CuO Nanoporous Photocatalytic Electrodes. *Materials* **2022**, *15*, 1489. [[CrossRef](#)] [[PubMed](#)]
34. Yang, L.; Liu, Z. Study on Light Intensity in the Process of Photocatalytic Degradation of Indoor Gaseous Formaldehyde for Saving Energy. *Energy Convers. Manag.* **2007**, *48*, 882–889. [[CrossRef](#)]
35. Sayyah, S.M.; Shaban, M.; Rabia, M. Electropolymerization of M-Toluidin on Platinum Electrode from Aqueous Acidic Solution and Character of the Obtained Polymer. *Adv. Polym. Technol.* **2018**, *37*, 126–136. [[CrossRef](#)]
36. Rabia, M.; Hadia, N.M.A.; Farid, O.M.; Abdelazeez, A.A.A.; Mohamed, S.H.; Shaban, M. Poly(m-Toluidine)/Rolled Graphene Oxide Nanocomposite Photocathode for Hydrogen Generation from Wastewater. *Int. J. Energy Res.* **2022**, *46*, 11943–11956. [[CrossRef](#)]
37. Sayyah, S.M.; Shaban, M.; Rabia, M. M-Toluidine Polymer Film Coated Platinum Electrode as a PH Sensor by Potentiometric Methods. *Sens. Lett.* **2015**, *13*, 961–966. [[CrossRef](#)]
38. Sayyah, S.M.; Shaban, M.; Rabia, M. A High-Sensitivity Potentiometric Mercuric Ion Sensor Based on m-Toluidine Films. *IEEE Sens. J.* **2016**, *16*, 1541–1548. [[CrossRef](#)]
39. Ragupathi, V.; Raja, M.A.; Panigrahi, P.; Ganapathi Subramaniam, N. CuO/g-C<sub>3</sub>N<sub>4</sub> Nanocomposite as Promising Photocatalyst for Photoelectrochemical Water Splitting. *Optik* **2020**, *208*, 164569. [[CrossRef](#)]
40. Masudy-Panah, S.; Moakhar, R.S.; Chua, C.S.; Tan, H.R.; Wong, T.I.; Chi, D.; Dalapati, G.K. Nanocrystal Engineering of Sputter-Grown CuO Photocathode for Visible-Light-Driven Electrochemical Water Splitting. *ACS Appl. Mater. Interfaces* **2016**, *8*, 1206–1213. [[CrossRef](#)]
41. Huang, X.; Zhang, M.; Sun, R.; Long, G.; Liu, Y.; Zhao, W. Enhanced Hydrogen Evolution from CuOx-C/TiO<sub>2</sub> with Multiple Electron Transport Pathways. *PLoS ONE* **2019**, *14*, e0215339. [[CrossRef](#)] [[PubMed](#)]
42. Li, J.; Jin, X.; Li, R.; Zhao, Y.; Wang, X.; Liu, X.; Jiao, H. Copper Oxide Nanowires for Efficient Photoelectrochemical Water Splitting. *Appl. Catal. B Environ.* **2019**, *240*, 1–8. [[CrossRef](#)]
43. Jin, L.; AlOtaibi, B.; Benetti, D.; Li, S.; Zhao, H.; Mi, Z.; Vomiero, A.; Rosei, F. Near-Infrared Colloidal Quantum Dots for Efficient and Durable Photoelectrochemical Solar-Driven Hydrogen Production. *Adv. Sci.* **2016**, *3*, 1500345. [[CrossRef](#)] [[PubMed](#)]
44. Baran Aydin, E. Fabrication and Characterization of CuO Nanostructures: Applications in Electrocatalytic Hydrogen Production. *Çukurova Univ. J. Fac. Eng. Archit.* **2020**, *35*, 127–138.
45. Ebaid, M.; Kang, J.-H.; Ryu, S.-W. Controlled Synthesis of GaN-Based Nanowires for Photoelectrochemical Water Splitting Applications. *Semicond. Sci. Technol.* **2016**, *32*, 013001. [[CrossRef](#)]

46. Sherman, B.D.; Ashford, D.L.; Lapides, A.M.; Sheridan, M.V.; Wee, K.-R.; Meyer, T.J. Light-Driven Water Splitting with a Molecular Electroassembly-Based Core/Shell Photoanode. *J. Phys. Chem. Lett.* **2015**, *6*, 3213–3217. [[CrossRef](#)]
47. Uchiyama, H.; Isobe, K.; Kozuka, H. Preparation of Porous CuO Films from Cu(NO<sub>3</sub>)<sub>2</sub> Aqueous Solutions Containing Poly(Vinylpyrrolidone) and Their Photocathodic Properties. *RSC Adv.* **2017**, *7*, 18014–18018. [[CrossRef](#)]
48. Liu, G.; Karuturi, S.K.; Chen, H.; Wang, D.; Ager, J.W.; Simonov, A.N.; Tricoli, A. Enhancement of the Photoelectrochemical Water Splitting by Perovskite BiFeO<sub>3</sub> via Interfacial Engineering. *Sol. Energy* **2020**, *202*, 198–203. [[CrossRef](#)]
49. Li, Z.; Feng, S.; Liu, S.; Li, X.; Wang, L.; Lu, W. A Three-Dimensional Interconnected Hierarchical FeOOH/TiO<sub>2</sub>/ZnO Nanostructural Photoanode for Enhancing the Performance of Photoelectrochemical Water Oxidation. *Nanoscale* **2015**, *7*, 19178–19183. [[CrossRef](#)]
50. Naldoni, A.; Guler, U.; Wang, Z.; Marelli, M.; Malara, F.; Meng, X.; Besteiro, L.V.; Govorov, A.O.; Kildishev, A.V.; Boltasseva, A.; et al. Broadband Hot-Electron Collection for Solar Water Splitting with Plasmonic Titanium Nitride. *Adv. Opt. Mater.* **2017**, *5*, 1601031. [[CrossRef](#)]
51. Wang, Z.; Cao, D.; Wen, L.; Xu, R.; Oberfell, M.; Mi, Y.; Zhan, Z.; Nasori, N.; Demsar, J.; Lei, Y. Manipulation of Charge Transfer and Transport in Plasmonic-Ferroelectric Hybrids for Photoelectrochemical Applications. *Nat. Commun.* **2016**, *7*, 10348. [[CrossRef](#)] [[PubMed](#)]
52. Freeman, E.; Kumar, S.; Thomas, S.R.; Pickering, H.; Fermin, D.J.; Eslava, S. PrFeO<sub>3</sub> Photocathodes Prepared through Spray Pyrolysis. *ChemElectroChem* **2020**, *7*, 1365–1372. [[CrossRef](#)]
53. Modibane, K.D.; Waleng, N.J.; Ramohlola, K.E.; Maponya, T.C.; Monama, G.R.; Makgopa, K.; Hato, M.J. Poly(3-Aminobenzoic Acid) Decorated with Cobalt Zeolitic Benzimidazolate Framework for Electrochemical Production of Clean Hydrogen. *Polymers* **2020**, *12*, 1581. [[CrossRef](#)] [[PubMed](#)]